



## A surface model for water and energy balance in cold regions accounting for vapor diffusion

1 Enkhbayar Dandar<sup>1,2,4</sup>, Maarten W.Saaltink<sup>2,3</sup>, Jesús Carrera<sup>1,3</sup>, Buyankhishig Nemer<sup>4</sup>

2 <sup>1</sup>Institute of Environmental Assessment and Water Research (IDAEA), CSIC, c/ Jordi Girona 18-26, Barcelona,08034, Spain

3 <sup>2</sup>GHS, Department of Civil and Environmental Engineering, Universitat Politecnica de Catalunya, UPC, Jordi Girona 1-3,  
4 Barcelona, 08034, Spain

5 <sup>3</sup>Associated Unit: Hydrogeology Group (UPC-CSIC)

6 <sup>4</sup>Department of Geology and Hydrogeology, School of Geology and Mining Engineering, MUST, Baga Toiruu 46-114,  
7 Ulaanbaatar, 14191,Mongolia

8 *Correspondence to:* Enkhbayar Dandar ([denkhbayar@gmail.com](mailto:denkhbayar@gmail.com))

9 **Abstract.** Computation of recharge in subarctic climate regions is complicated by phase change and permafrost, causing  
10 conventional conceptual land surface models to be inaccurate. We conjecture that large vapor pressure gradients, driven by  
11 the large temperature difference between the soil surface and the thawing permafrost active layer, may cause a significant  
12 water and energy transfer during late spring and early summer. To analyze this conjecture, we develop a two-compartment  
13 water and energy balance model that accounts for freezing and melting and includes vapor diffusion as a water and energy  
14 transfer mechanism. It also accounts for the effect of slope orientation on radiation, which may be important for high latitude  
15 mountain areas. We apply this model to weather data from the Terelj station (Mongolia). We find that vapor diffusion plays  
16 an important quantitative role in the energy balance and a relevant qualitative role in the water balance. Except for snowmelt  
17 and a few large precipitation events, most of the continuous recharge is driven by vapor diffusion fluxes. Large vapor fluxes  
18 occur during spring and early summer, when surface temperatures are moderate, but the subsoil remains cold, creating large  
19 downwards vapor pressure gradients. Temperature gradients reverse in fall and early winter, but the vapor diffusion fluxes  
20 do not, because of the small vapor pressure differences at low temperature. The downwards latent heat flux associated to  
21 vapor diffusion is essential for the thawing of the active layer. On a yearly basis, it is largely compensated by heat  
22 conduction, which is much larger than in temperate regions and upwards on average. Furthermore, we find that total surface  
23 runoff is small and concentrated at the beginning of spring due to snowmelt. Recharge is relatively high and delayed with  
24 respect to snowmelt because a portion of it is associated to thawing at depth, which may occur much later.

25  
26



## 27 1. Introduction

28 This work is motivated by the assessment of water resources in the Upper Tuul River basin, around Ulaanbaatar (Mongolia)  
29 and, in general, by subarctic continental climate regions, characterized by very low temperatures, low rainfall and, yet,  
30 sizable runoff. This causes such regions to fall very low in the Budyko curve (see, e.g., Figure C1 of Hanasaki et al., 2008).  
31 That is, total runoff is much larger than what would be expected in terms of potential evapotranspiration and rainfall.

32 We conjecture that increased runoff may be caused by condensation (deposition) of air moisture. Condensation and freezing  
33 may be especially significant during spring when air temperature and moisture increase, which drives water vapor to the cold  
34 soil. Later in spring, the soil surface warms up, which causes the active permafrost layer to start thawing while maintaining  
35 large temperature gradients, which should drive a significant water (and latent heat) flux down wards by vapor diffusion.  
36 This mechanism was proposed by Shvetzov (1978) and it is also mentioned by Gusev and Nanosova (2002), but has never  
37 been analyzed. Since moisture condensation data are not available in such regions, a quantitative analysis requires the use of  
38 mathematical models. Moreover, since phase changes and vapor diffusion are driven by energy availability and temperature  
39 differences, these models must consider water and energy balances.

40 Water and energy balances are the basic building blocks for any hydrological model. Many types of models are used for  
41 modeling phenomena such as recharge, evapotranspiration and water flow in soil. We can divide them into FE/FD (Finite  
42 Element/Finite Difference) models and integrated models. FE/FD models use more or less finely discretized grids for solving  
43 the partial differential equations governing multiphase non-isothermal flow in unsaturated soils. Examples are  
44 CODEBRIGHT (Olivella et al., 1996), COUPMODEL (Jansson and Moon, 2001), HYDRUS (Šimůnek et al., 2008), and  
45 SHAW (Flerchinger, 2017). Many of them also consider ice, heat exchange and vapor diffusion. They have been extensively  
46 used to analyze permafrost dynamics (e.g., McKenzie and Voss, 2013), but they require detailed input parameters, which are  
47 scarce for subarctic regions such as the Upper Tuul River basin, and are hard to interpret. Therefore, integrated models may  
48 be more appropriate for our case.

49 Integrated models calculate the basic terms of the water balance, such as stored soil water, evapotranspiration and surface  
50 runoff, over vertically integrated portions of the domain (representing canopy, soil surface and/or other parts of the soil).  
51 These models receive different names depending on the branch of hydrology (or sister sciences) of the author. At the  
52 watershed scale, they are called “water balance models” (Yates, 1996) and “large area hydrological models” (Arnold et al.,  
53 1998). When applied to even larger (up to global) scales, they are also called “global hydrological models” by hydrologists,  
54 who emphasize water balance, or “land surface models” by climatologists, who emphasize the energy balance as well  
55 (Haddeland et al., 2011). Well-known examples at the watershed scale, are WATBAL (Yates, 1996) and SWAT (e.g.,  
56 Arnold et al., 1998; Hülsmann et al., 2015). In its original form, SWAT calculates snowmelt by means of a water balance of  
57 the snow cover and a so called temperature-index method that estimates the snow cover temperature from previous ones and  
58 air temperature. Some later versions of SWAT use energy balances of the snow cover instead of the temperature-index  
59 method (e.g., Fuka et al., 2012). SWAT has been recently extended by considering energy balances in the soil as well (Qi et  
60 al., 2016), but only considers conduction as a mechanism for heat transport in the soil. None of these integrated models



61 simulate vapor diffusion in the soil. For our purposes we need to take into account vapor diffusion flux in both the water and  
62 the energy balance of the soil.

63 The aim of this work is to assess the importance of vapor diffusion in cold and semi-arid regions and, so, obtain a better  
64 understanding of the hydrological processes in such regions. We do this by developing a hydrological scheme that consider  
65 both water and energy balances and accounts for vapor diffusion as well as other processes that are relevant for subarctic  
66 climates, including the effect of slope on radiation.

## 67 2. Methodology

### 68 2.1. Model description

69 Water and energy balances in land surface hydrological models are typically expressed on one or two layers. The top layer  
70 usually extends to root depth, where (shallow rooted) plants can extract water and daily temperature fluctuations are  
71 dampened. We formulate the balances over two layers (see Figure 1) because we are interested in water and energy  
72 dynamics including seasonal fluctuations. The surface layer extends some 16 cm, so as to accommodate the roots of typical  
73 grass in the Upper Tuul basin and to dampen daily temperature fluctuations. The subsoil (with length  $L_{ss}$ ) layer extends some  
74 150 cm and accommodates the “active” layer that freezes and thaws seasonally. The input and output terms for the water  
75 balance of the surface layer include precipitation (as rain or snow), evapotranspiration (including both ice deposition and  
76 sublimation), infiltration into the subsoil and vapor diffusion to or into the subsoil. Those for the subsoil are infiltration,  
77 vapor diffusion from the surface and recharge to the aquifer. The energy balance considers solar radiation, latent and sensible  
78 heat fluxes, heat conduction between the two layers and energy released due to phase changes. The model also takes into  
79 account the slope of the surface. The above fluxes can be written as a function of meteorological data and two state  
80 variables: mass of water ( $\text{kg m}^{-2}$ ) and energy ( $\text{J m}^{-2}$ ). Details of each mass balance term are given below.

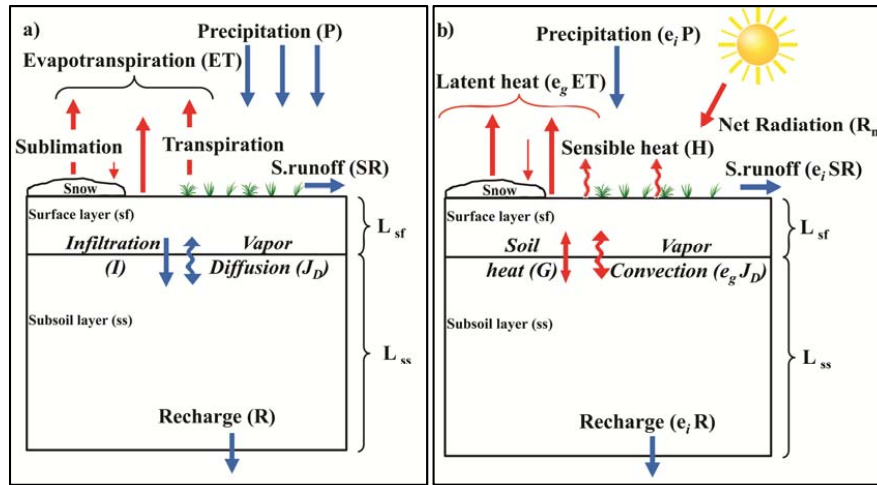


Figure 1. Schematic diagram of the water balance (a) and energy balance (b) models

81  
 82

## 83 2.2. Water balance

84 The water balance for the surface and the subsoil layers can be formulated as:

$$\frac{\partial m_{sf}}{\partial t} = P - ET_{sf} - I - SR - J_D \quad (1)$$

$$\frac{\partial m_{ss}}{\partial t} = I - ET_{ss} - R + J_D \quad (2)$$

85 where subscripts “sf” and “ss” refer to surface and subsoil layers, respectively,  $m$  is the mass of water (liquid or ice) ( $\text{kg m}^{-2}$ ), and fluxes (all in  $\text{kg m}^{-2} \text{s}^{-1}$ ) include precipitation ( $P$ ), evapotranspiration ( $ET$ ), infiltration ( $I$ , positive downwards),  
 86 surface runoff ( $SR$ ), vapor diffusion ( $J_D$ , positive downwards), and recharge ( $R$ ).  
 87

88 Evapotranspiration is commonly used to describe both evaporation and transpiration (Brutsaert, 1982), including  
 89 sublimation, i.e., the direct conversion of ice to water vapor (Zhang et al., 2004).  $ET$  is usually the most important term for  
 90 returning energy to the atmosphere. Traditional methods for estimating evapotranspiration can be divided into those that use  
 91 temperature (Hargreaves and Samani, 1985), radiation (Priestley and Taylor, 1972) and an aerodynamic approach  
 92 (McMahon et al., 2013 and Katul et al., 1992). We chose the latter, because in dry climates  $ET$  is controlled by water  
 93 availability rather than incoming radiation. The aerodynamic method is based on Dalton law, which establishes that  $ET$  is  
 94 proportional to the difference of vapor pressures between air and soil. It is the basis of the method of Penman (1948) and has  
 95 been used to estimate evaporation from water surfaces (Rosenberg et al., 1983; Xu and Singh, 2002), or bare soil (Ripple et  
 96 al., 1970) and evapotranspiration from vegetated surfaces (Blad and Rosenberg, 1976). We assume that one part of the water  
 97 evaporates from the soil surface controlled by an aerodynamic resistance and another part evaporates through plant



98 transpiration controlled by both aerodynamic and stomata resistance. Moreover, we distinguish between plant transpiration  
 99 from the soil surface and the subsoil. We express ET from soil surface and subsoil as:

$$ET_{sf} = \frac{M}{RT_{air}} \left[ \frac{1}{r_a + r_s} \alpha \beta + \frac{1}{r_a} (1 - \beta) \right] f_{sf} [p_{v,sf} - p_{v,air}] \quad (3)$$

$$ET_{ss} = \frac{M}{RT_{air}} \left[ \frac{1}{r_a + r_s} (1 - \alpha) \beta \right] f_{ss} [p_{v,ss} - p_{v,air}] \quad (4)$$

100 where  $M$  is the molar mass of water ( $0.018 \text{ kg mol}^{-1}$ ),  $R$  is the gas constant ( $8.314 \text{ J mol}^{-1} \text{ K}^{-1}$ ),  $T_{air}$  is the air temperature (K),  
 101  $r_a$  and  $r_s$  are the aerodynamic and stomata resistances, respectively ( $\text{s m}^{-1}$ ),  $\alpha$  is the fraction of total transpiration from the  
 102 surface layer and  $\beta$  is the fraction of vegetation cover. When the soil is frozen, no transpirations is assumed and  $\alpha$  and  $\beta$  are  
 103 given a zero value. Factor,  $f$ , represents the reduction of evaporation due to the lack of water in the surface and subsoil layers  
 104 (see below),  $p_{v,sf}$  and  $p_{v,ss}$  are the saturated vapor pressures (Pa) at the surface and subsoil layers and  $p_{v,air}$  is the actual  
 105 vapor pressure in the atmosphere (Pa). The actual vapor pressure can be calculated from the relative humidity and saturated  
 106 vapor pressure ( $p_{v,sat}$ ), which we computed with Murray's (1967) equation as a function of temperature.  
 107 The aerodynamic resistance,  $r_a$ , describes the resistance from the vegetation upward and involves friction from air flowing  
 108 over vegetative surfaces whereas the stomata surface resistance,  $r_s$ , describes the resistance of vapor flow through stomata,  
 109 total leaf area and evaporating soil surface (Shuttleworth, 1979). A general form for the aerodynamic resistance to  
 110 evapotranspiration (or sublimation) and sensible heat is (Evetts et al., 2011):

$$r_a = \frac{1}{k^2 u_z} \left[ \ln \left( \frac{z}{z_0} \right) \right]^2 \quad (5)$$

111 where  $z$  is height at which wind speed, temperature and relative humidity are measured (m),  $z_0$  is the roughness length (m),  $k$   
 112 is the von Karman's constant ( $k = 0.4$ ) and  $u_z$  is the wind speed ( $\text{m s}^{-1}$ ). The roughness length can vary over five orders of  
 113 magnitude (from  $10^{-5} \text{ m}$  for very smooth water surfaces to several meters for forests and urban areas) and increases gradually  
 114 with increasing height of roughness elements (Arya, 2001). The stomata surface resistance can be calculated by (Allen et al.,  
 115 1998):

$$r_s = \frac{r_1}{0.5 \text{ LAI}} \quad (6)$$

116 where  $r_1$  is the bulk stomata resistance of a well-illuminated leaf ( $\text{s m}^{-1}$ ). Monteith and Unsworth (1990) suggest that  $r_1 = 100$   
 117  $\text{s m}^{-1}$  for grassland. LAI is the leaf area index (leaf area per unit soil surface area).

118 Factor,  $f$ , in equations (3) and (4) expresses the decreases of ET with water content in the surface and subsoil layers,  
 119 according to:



$$f_{sf/ss} = \begin{cases} 1 & \text{if } m_{sf/ss} > m_{sf/ss}^{fc} \\ \frac{m_{sf/ss} - m_{sf/ss}^{wp}}{m_{sf/ss}^{fc} - m_{sf/ss}^{wp}} & \text{if } m_{sf/ss} < m_{sf/ss}^{fc} \\ 0 & \text{otherwise} \end{cases} \quad (7)$$

120 where superscripts fc and wp refer to field capacity and wilting point, respectively.

121 For the calculation of infiltration (I) we assume that it is limited by a maximum infiltration capacity, and that only liquid  
 122 water exceeding the field capacity can infiltrate. Then, for a time step  $\Delta t$  the infiltration can be formulated as:

$$I^{k+1} = \max \left( 0, \left[ \min \left( \left( \frac{m_{sf}^{k+1} - m_{sf}^{wp}}{\Delta t} + P - ET_{sf} - J_D \right), I_{max}, m_{sf,l} \right) \right] \right) \quad (8)$$

123 where  $m_{sf}^{k+1}$  is the mass of water in the surface layer at a present time step and  $m_{sf,l}$  is the liquid mass of water in the surface  
 124 layer ( $\text{kg m}^{-2}$ ). The maximum infiltration ( $I_{max}$ ) equals the saturated hydraulic conductivity ( $K_{sat}$ ).

125 In a similar way we calculate surface runoff (SR) by assuming that only water exceeding the maximum water content in the  
 126 surface layer ( $m_{sf}^{\phi}$ ) can runoff, where  $m_{sf}^{\phi}$  ( $\text{kg m}^{-2}$ ) equals the porosity ( $\phi$ ) multiplied by water density and length of the soil  
 127 surface ( $L_{sf}$ ). For the calculation of recharge (R) we assume that only liquid water exceeding the field capacity in the subsoil  
 128 layer can percolate to the aquifer.

129 Vapor diffusion using Fick's Law, is written as:

$$J_D = \frac{M}{RT_{sf}} \frac{D}{L_{sf}} \frac{m_{sf}^{\phi} - m_{sf}}{m_{sf}^{\phi}} [p_{v,sf} - p_{v,ss}] \quad (9)$$

130 where D is the diffusion coefficient ( $\text{m}^2 \text{s}^{-1}$ ),  $T_{sf}$  is the temperature of the surface layer (K),  $L_{sf}$  is the surface layer's length  
 131 (m). Note that we use  $L_{sf}$  as length between the two layers rather than  $(L_{sf} + L_{ss})/2$  because temperature gradients, which  
 132 control vapor pressure, are expected to be largest near the soil surface. The value to be adopted for the diffusion coefficient  
 133 deserves some discussion. The diffusion coefficient of water vapor in air is  $0.3 \cdot 10^{-4} \text{ m}^2 \text{ s}^{-1}$  (Cussler, 1997). This value should  
 134 be reduced due to reduced open area and tortuosity in a porous medium. However, for reasons that are subject to debate (Ho  
 135 and Webb, 2006), vapor diffusion is enhanced (Cass et al., 1984). Gran et al., (2011b) used values above  $2 \cdot 10^{-4} \text{ m}^2 \text{ s}^{-1}$ . Given  
 136 these uncertainties we have adopted  $10^{-4} \text{ m}^2 \text{ s}^{-1}$  as base value, and then analyzed the sensitivity of the model to this  
 137 parameter.

138

139

### 140 2.3. Energy balance

141 Energy balance for the two layers is written as:



$$\frac{\partial U_{sf}}{\partial t} = e_{i/l}P - e_g ET_{sf} - (e_g - e_l)ET_{ss} - e_l I - e_l SR + R_n - H - G - e_g J_D \quad (10)$$

$$\frac{\partial U_{ss}}{\partial t} = e_l I - e_l ET_{ss} - e_l R + G + e_g J_D \quad (11)$$

142 where  $U$  is the total energy of each layer ( $J m^{-2}$ ),  $R_n$  is the net radiation ( $J m^{-2} s^{-1}$ ),  $H$  is the sensible heat flux ( $J m^{-2} s^{-1}$ ) and  $G$   
 143 is the heat conduction ( $J m^{-2} s^{-1}$ ) between surface and subsoil. Advective heat fluxes include the fluxes of water, ice (snow)  
 144 or vapor ( $P$ ,  $ET$ ,  $SR$ ,  $I$ ,  $J$ ,  $R$ ) multiplied by the corresponding internal energies of liquid water, ice or vapor ( $e_l$ ,  $e_i$ ,  $e_g$  ( $J$   
 145  $kg^{-1}$ )), which are linear functions of temperature. Although a distinction is made between evapotranspiration from the  
 146 surface and the subsoil ( $ET_{sf}$  and  $ET_{ss}$ ), equations (10) and (11) assume that the heat loss occurs only at the surface because  
 147 the actual phase change takes place in the plant, which is part of the surface layer.  
 148 The total energy ( $U$ ) is a sum of energy for liquid water, ice and solid (Figure 2):

$$U = me = m_l e_l + m_i e_i + m_s e_s \quad (12)$$

149 where subscript  $s$  presents the solid part of the soil layers. During melting or freezing, the temperature is fixed at the melting  
 150 temperature of  $0^\circ C$  while at higher temperature all water is liquid ( $m = m_l$ ) and at lower temperature all water is ice  
 151 ( $m = m_i$ ). Therefore, we can calculate the temperature and mass of ice and water as a function of  $U$  and  $m$  as:

$$T = \frac{U + m\Lambda_{melt}}{m c_i + m_s c_s} \quad \text{and} \quad m = m_i \quad \text{if} \quad -m\Lambda_{melt} > U \quad (13)$$

$$T = 0 \quad \text{and} \quad m_i = -\frac{U}{\Lambda_{melt}}; \quad m_l = m - m_i \quad \text{if} \quad -m\Lambda_{melt} < U < 0 \quad (14)$$

$$T = \frac{U}{m c_l + m_s c_s} \quad \text{and} \quad m = m_l \quad \text{if} \quad U > 0 \quad (15)$$

152 where  $\Lambda_{melt}$  is the melting heat ( $3.34 \cdot 10^5 J kg^{-1}$ ),  $c_l$  is specific heat of water ( $4184 J kg^{-1} ^\circ C^{-1}$ ),  $c_i$  is specific heat of ice ( $2092$   
 153  $J kg^{-1} ^\circ C^{-1}$ ) and  $c_s$  is specific heat of soil ( $843 J kg^{-1} ^\circ C^{-1}$ ). Equations (13) to (14) are also illustrated by Figure 2.

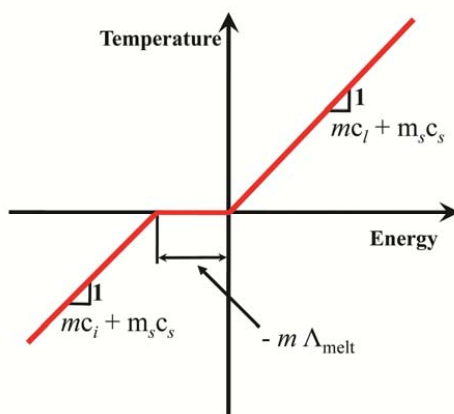


Figure 2. Temperature versus total energy

154  
 155

156 **Radiation**

157 Radiation is the main energy input for land surface models. Hence, it is not surprising that it has received a lot of attention.  
 158 We follow a somewhat modified version of the approaches of Tian et al., (2001) and Allen et al., (2006) and divide radiation  
 159 between shortwave, received from the sun, and longwave radiation, emitted by the Earth and the atmosphere. Net radiation  
 160 ( $R_n$ ) is the sum of the net shortwave radiation ( $R_{ns}$ ) and the net longwave radiation ( $R_{nl}$ ):

$$R_n = R_{ns} + R_{nl} = (1 - A)R_S + R_{L,down} + R_{L,down} \quad (16)$$

161 where  $A$  is the albedo, fraction of solar radiation ( $R_S$ ) that is reflected by the surface. The albedo depends on surface types  
 162 (small for vegetated surface and high values for snow). In our model the albedo was determined from data on snow depth.  
 163 However, this could easily be changed (e.g., to a dependence on mass of ice in the subsoil), when no snow depth data are  
 164 available. The net longwave radiation is equal to the received (downward,  $R_{L,down}$ ) minus the emitted ( $R_{L,up}$ ) radiation.

165 **Solar radiation on a horizontal and on an inclined surface**

166 The solar radiation on a horizontal surface ( $R_{S,hor}$ ) is measured or can be calculated from the atmospheric transmissivity  
 167 ( $\tau_a$ ), which is the fraction of extraterrestrial solar radiation (easy to compute, see Appendix A) that makes it to the land  
 168 surface. Atmospheric transmissivities are highly sensitive to cloudiness and moisture content. It can be estimated from the  
 169 relative sunshine hours (Allen et al., 1998) or through the method of Hargreaves and Allen (2003):

$$\tau_a = K_H \sqrt{T_{air}^{max} - T_{air}^{min}} \quad (17)$$

170 where  $T_{air}^{max}$  and  $T_{air}^{min}$  are the daily maximum and minimum air temperature and  $K_H$  is an empirical constant. Allen et al.,  
 171 (1998) recommends  $K_H = 0.16$  for interior and  $K_H = 0.19$  for coastal regions.





172 Shortwave radiation may reach the land surface directly from the sun, reflected by the surrounding or scattered by the  
 173 atmosphere (diffuse solar radiation). The distinction is relevant for inclined surfaces in the shade, which only receive  
 174 reflected and diffuse solar radiation. Numerous relations can be found in the literature (Noorian et al., 2008) to estimate the  
 175 fraction of diffuse radiation over the total solar radiation ( $f_{dif}$ ). We adopted the one of Boland et al., (2008), which is simple  
 176 and statistically sound:

$$f_{dif} = \frac{1}{1 + \exp(8.6\tau_a - 5)} \quad (18)$$

177 Solar radiation on an inclined surface can be calculated from the solar radiation on a horizontal surface by means of the  
 178 following expression (e.g., Tian et al., 2001):

$$R_S = R_{S,hor} \left[ (1 - f_{dif}) \frac{\max(\mathbf{p}^T \mathbf{s}, 0)}{s_{up}} + f_{dif} f_{sv} + A(1 - f_{sv}) \right] \quad (19)$$

179 where  $f_{sv}$  is the sky view factor (see equation A14 in the Appendix). The first term represents the direct solar radiation, the  
 180 second term the diffuse radiation and the third term the solar radiation reflected from the surroundings. Definitions of  $\mathbf{p}^T \mathbf{s}$   
 181 and  $s_{up}$  are shown in the Appendix (equations A1 and A2). To perform daily energy balances, we calculate the daily  
 182 averaged solar radiation on an inclined surface, assuming the atmospheric transmissivity ( $\tau_a$ ) to be constant during the day, as  
 183 follows:

$$R_S = \left[ (1 - f_{dif}) \frac{\int_{-\omega_{ss}}^{\omega_{ss}} \max(\mathbf{p}^T \mathbf{s}, 0) dt}{\int_{-\omega_{ss}}^{\omega_{ss}} s_{up} dt} + f_{dif} f_{sv} + A(1 - f_{sv}) \right] R_{S,hor} \quad (20)$$

184 where  $\omega_{ss}$  is the sunset angle, the integrals of  $s_{up}$  and  $\max(\mathbf{p}^T \mathbf{s}, 0)$  are given by equations A6 and A13 of the Appendix.

### 185 *Longwave radiation*

186 Longwave radiation appears simple, but actual parameterization is hard (Herrero and Polo, 2012; Zabel et al., 2012). Upward  
 187 longwave radiation is calculated from Stefan-Boltzmann law:

$$R_{L,up} = -\varepsilon_s \sigma T_{sf}^4 \quad (21)$$

188 where  $\varepsilon_s$  is the surface emissivity,  $\sigma$  is the Stefan-Boltzmann constant ( $5.7 \cdot 10^{-8} \text{ J s}^{-1} \text{ m}^{-2} \text{ K}^{-4}$ ) and  $T_{sf}$  is the surface temperature  
 189 (K). The soil surface emissivity is usually close to 1 (Saito and Šimůnek, 2009). However, small changes in  $\varepsilon_s$  may cause an  
 190 imbalance between upwards and downwards longwave radiation balance, thus having a large effect on net radiation. We  
 191 adopted a constant value of 0.94, but also tested 0.99 for sensitivity analysis purposes.

192 The Earth's surface also receives longwave radiation emitted by the atmosphere and surrounding surfaces. It can be  
 193 calculated from the same law:

$$R_{L,down} = f_{sv} \varepsilon_a \sigma T_{air}^4 - (1 - f_{sv}) R_{L,up} \quad (22)$$



194 where  $\epsilon_a$  is the emissivity of the atmosphere and  $T_{\text{air}}$  the absolute temperature of the atmosphere. Note that a fraction equal  
 195 to the sky view factor ( $f_{sv}$ ) originates from the atmosphere and another part ( $1-f_{sv}$ ) from the surroundings.

196 Clear sky emissivity is obtained from the empirical expression of Brutsaert (1975):

$$\epsilon_{\text{air.cs}} = 1.24 \left( \frac{P_{v,\text{air}}}{T_{\text{air}}} \right)^{1/7} \quad (23)$$

197 The cloudy sky emissivity ( $\epsilon_a$ ) is obtained from  $\epsilon_{\text{air.cs}}$  using the expression that Sicart et al., (2006) derived empirically for a  
 198 subarctic continental climate in Yukon (Canada):

$$\epsilon_a = \epsilon_{\text{air.cs}} (1 + 0.44h_r - 0.18\tau_a) \quad (24)$$

199 where  $h_r$  is relative humidity.

#### 200 *Sensible heat*

201 The sensible heat flux is calculated using the aerodynamic resistance ( $r_a$ ) and soil surface resistance ( $r_{\text{sf}}$ ):

$$H = \frac{\rho_a c_a}{r_a + r_{\text{sf}}} (T_{\text{sf}} - T_{\text{air}}) \quad (25)$$

202 where  $\rho_a$  is the air density ( $1.22 \text{ kg m}^{-3}$ ) and  $c_a$  is the specific heat of air ( $1013 \text{ J kg}^{-1} \text{ K}^{-1}$ ). The soil surface resistance,  $r_{\text{sf}}$ , is  
 203 calculated from the thermal conductivity of the soil:

$$r_{\text{sf}} = \frac{0.5 L_{\text{sf}} \rho_a c_a}{\lambda} \quad (26)$$

204 where  $\lambda$  is the thermal conductivity of the soil.

#### 205 *Heat conduction*

206 Heat conduction of soil can be calculated from Fourier's Law as:

$$G = \frac{\lambda}{(0.5 L_{\text{sf}} + 0.5 L_{\text{ss}})} (T_{\text{sf}} - T_{\text{ss}}) \quad (27)$$

207 where  $\lambda$  is the soil thermal conductivity ( $\lambda = \lambda_i^\phi \lambda_s^{1-\phi}$ ), where  $\phi$  is the porosity,  $\lambda_s$  is the thermal conductivity of the solid  
 208 particles, and  $\lambda_i$  is the thermal conductivity of ice,  $\lambda_i$ , when water is frozen or that of liquid water,  $\lambda_l$ , otherwise (Côté and  
 209 Konrad, 2005).

#### 210 **2.4. Numerical solution and implementation**

211 We solve the water and energy balance equations (Eqs. (1),(2), (10) and (11), respectively) using a semi-implicit finite  
 212 differences scheme with a time step of one day. The term semi-implicit means that all variables are treated explicitly (i.e.,  
 213 using the values from the previous day), with two exceptions to ensure stability. First, vapor pressures in equations (3), (4)



214 and (9) are linearized and treated implicitly (that is,  $p_{v,sf}^{k+1} - p_{v,air} = (T_{sf}^{k+1} - T_{air})\Delta + (1 - h_r)p_{v,sat}$ , where  $\Delta$  is the slope  
215 of the saturation vapor pressure curve (Pa °C<sup>-1</sup>). This type of linearization is frequent (e.g., Penman, 1948) because vapor  
216 pressure is highly sensitive to temperature and treating it explicitly may cause instability. Second, we perform a preliminary  
217 water balance to approximate the water available for evaporation, this is followed by the energy balance which yields not  
218 only energy and temperature, but also actual evaporation, that is used for the final water balance.  
219 The algorithm was implemented in a spreadsheet that is available for the cases discussed below at  
220 <http://h2ogeo.upc.edu/es/investigacion-hidrologia-subterrania/software>.  
221 All terms but the vapor diffusion, in the water (section 2.2) and energy (section 2.3) balances have been extensively tested  
222 (see introduction). We test the validity of our formulation in the Appendix B.

## 223 2.5. Data of meteorological stations and parameters

224 The model was tested using meteorological data from 2000 through 2004 of the Terelj station (elevation 1540 m, 47.98N,  
225 107.45E), located in northern Mongolia some 40 km east of Ulaanbaatar. This station records daily meteorological data  
226 (maximum and minimum T, precipitation, snow depth, wind and relative humidity) provided by the Institute of Meteorology  
227 and Hydrology of Mongolia. The area is mountainous with grassland and forest of Larix and Pinus. Forests dominate the  
228 north face of mountains while grassland dominates the south face of mountains and flat areas (Dulamsuren et al., 2008;  
229 Ishikawa et al., 2005). The region contains discontinuous and sparsely insular permafrost (Gravis et al., 1972; Sharkhuu,  
230 2003; Jambaljav et al., 2008).

231 The average daily maximum and minimum air temperature is 5.06°C and -11.5°C, respectively. Mean air temperature  
232 averaged -3.2°C for the studied period. Annual precipitation averaged 334 mm/year, with 80% falling between June and  
233 September. Snow usually falls between mid-October and mid-April, with a maximum thickness of 31 cm. The average wind  
234 speed is 1.5 m/s and average relative humidity 70.12%.

235 We used parameters from the literature (Table 1) to define a base model that assumes that the surface is horizontal and  
236 covered by grass. Jambaljav et al., (2008) noted that the north and south facing slopes of mountains in the Terelj area are  
237 about 10-40°. Therefore, for the sensitivity analysis, we considered north and south faces with a slope of 20 degrees.  
238 Tuvshinjargal et al., (2004) used an albedo of 0.21 for grass meadow to calculate the surface energy balance. There are no  
239 other data for albedo from this area, especially snow albedo. The albedo (A) was taken from Oke (1987) as 0.6 during  
240 periods with snow cover and 0.23 for grass and soil surface. Most surfaces have emissivities larger than 0.9 (Arya, 2001).  
241 So, we used  $\epsilon_s=0.94$  for the base model. We assumed that all the roots of grass are in the surface layer ( $L_{sf}$ ) which means the  
242 evapotranspiration only occurs from the surface layer. Thus, we used  $\alpha$  equal to 1.

243 The surface roughness length ( $z_0$ ) is defined by surface types such as soil, vegetation and snow. We used  $z_0=0.04$  for grass  
244 and  $z_0=0.002$  for snow surface (see figure 10.5 of Arya, 2001). The leaf area index (LAI) is defined by vegetation types.  
245 Asner et al., (2003) give LAI of 2.1 m<sup>2</sup>m<sup>-2</sup> for grass. According to the National Soil Atlas of Mongolia (1981), the soil of the  
246 study area belongs to the Gleysols-umbrisoland Cryosols-leptic type. The soil texture is mainly a silt-clay-loam. The wilting  
247 point ( $\theta^{wp}$ ), field capacity ( $\theta^c$ ), porosity ( $\phi$ ) and saturated hydraulic conductivity ( $K_{sat}$ ) are 0.11, 0.342, 0.365 and 4.2·10<sup>-7</sup> m



248  $s^{-1}$ , respectively, and were obtained from Schroeder et al., (1994). Length of the surface layer ( $L_{sf}$ ) and subsoil layer are of  
 249 0.16 m and 1.5 m, respectively. Thermal conductivities were obtained from Bristow (2002).

250 For the sensitivity runs we changed eight parameters: dip of the surface ( $\theta$ ), roughness length ( $z_0$ ), soil emissivity ( $\epsilon_s$ ),  
 251 saturated conductivity ( $K_{sat}$ ), wilting point ( $\theta^{wp}$ ), vapor diffusion coefficient (D), surface length ( $L_{sf}$ ) and subsoil length ( $L_{ss}$ ).

252 **Table1.** Parameter and values for Base model

Parameters	Value	Units	Reference
Slope ( $\theta$ )	0	degree	
Latitude ( $\phi$ )	48	degree	
Albedo (A)	0.23 for grass and soil 0.6 for snow	-	Oke, 1987
Soil emissivity ( $\epsilon_s$ )	0.94	-	Arya, 2001
Fraction of transpiration ( $\alpha$ )	1	-	
Vegetation cover ( $\beta$ )	0.6	-	Dulamsuren et al., 2008
Leaf area index (LAI)	2.1 for grass	$m^2 m^{-2}$	Asner et al., 2003
Surface roughness length ( $z_0$ )	0.04 for grass 0.002 for snow	m	Arya, 2001
Diffusion coefficient (D)	$10^{-4}$	$m^2 s^{-1}$	
Field capacity ( $\theta^c$ )	0.342	$m^3 m^{-3}$	Schroeder et al, 1994
Wilting point ( $\theta^{wp}$ )	0.11	$m^3 m^{-3}$	Schroeder et al, 1994
Porosity ( $\phi$ )	0.365	-	Schroeder et al, 1994
Saturated hydraulic conductivity ( $K_{sat}$ )	$4.2 \cdot 10^{-7}$	$m s^{-1}$	Schroeder et al, 1994
Surface depth ( $L_{sf}$ )	0.16	m	
Subsoil depth ( $L_{ss}$ )	1.5	m	
Thermal conductivity ( $\lambda$ )	2.9 for soil 0.57 for water 2.2 for ice	$J s^{-1} m^{-1} K^{-1}$	Bristow (2002)

### 253 3. Results

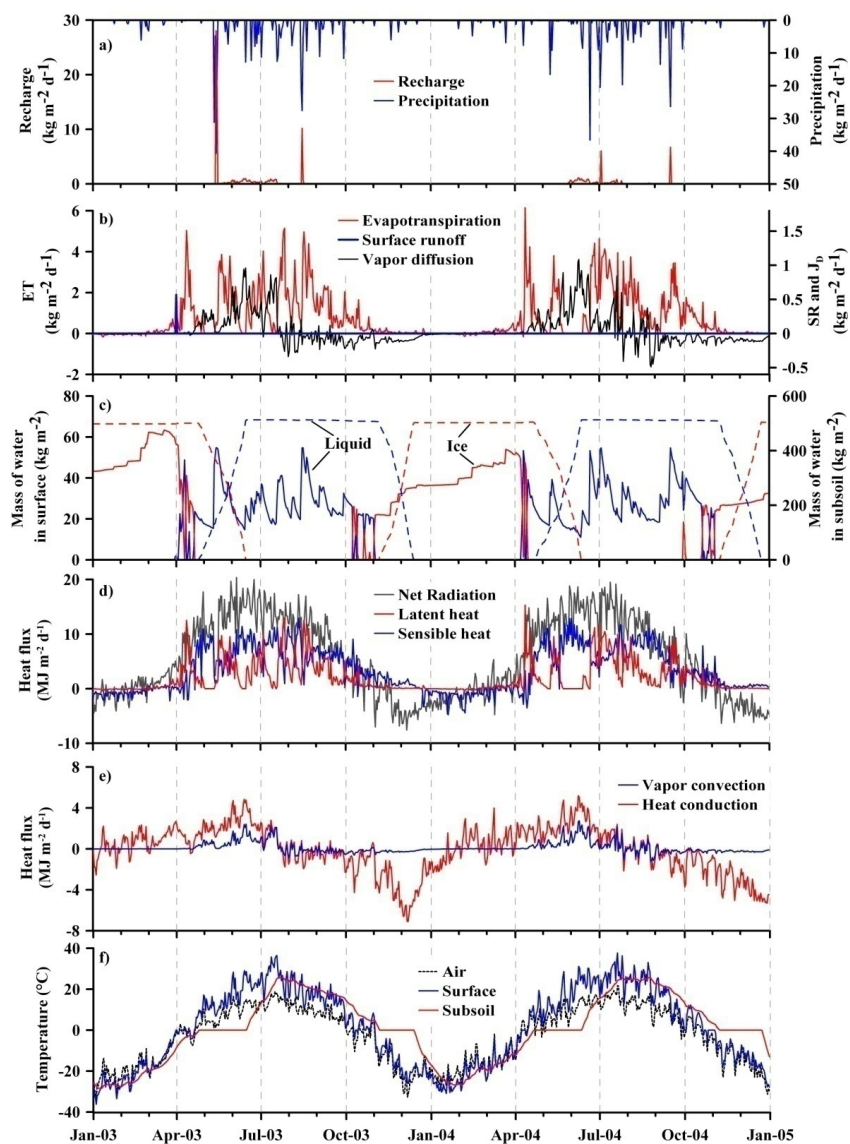
254 Results are summarized in Figure 3, which displays the evolution of the water fluxes (precipitation, evapotranspiration,  
 255 recharge, surface runoff and vapor diffusion), water contents, heat fluxes (net radiation, latent heat, sensible heat, vapor  
 256 convection and heat conduction) and temperature (air, surface and subsoil) of the base model during the last two years. Table  
 257 2 and 3 summarize the balances averaged over the 5 years for the base model and for the sensitivity.

258 Direct surface runoff is very small. Figure 3.b only shows some surface runoff at the beginning of April 2003 during  
 259 snowmelt. No surface runoff occurred during the snowmelt of 2004 probably because the accumulated snow on the surface  
 260 was small that year. The sensitivity analysis suggests that the limiting factor is the infiltration capacity. When saturated  
 261 hydraulic conductivity is reduced by a factor of 10, direct surface runoff increases dramatically and infiltration reduces. The  
 262 reduced infiltration also implies increased ET, so that the overall runoff (SR plus recharge) is also reduced. The small  
 263 surface runoff is consistent with the lack of very intense rainfall events and with the absence of indications of surface  
 264 erosion.

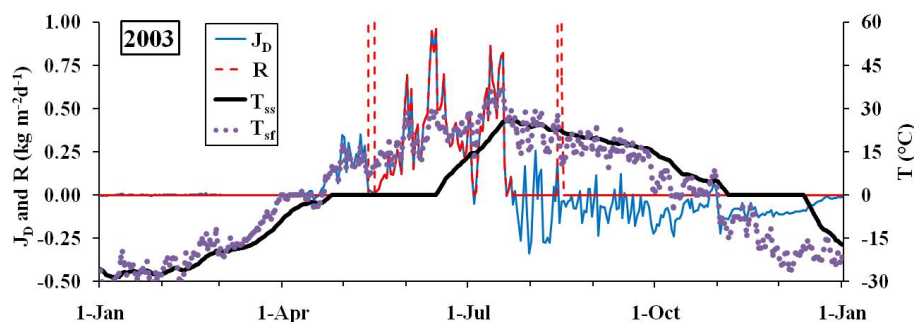


265 Infiltration and recharge are also relatively low. Infiltration occurs mainly after heavy rainfall events and it is not shown in  
266 figure 3 because similar pattern as recharge. Most infiltration transforms into recharge because, in the absence of deep rooted  
267 plants, the subsoil is always close to field capacity. Recharge from rainfall infiltration can vary a lot from year to year, due to  
268 the irregular occurrence of heavy rainfall events. However, a significant amount of recharge occurs throughout the spring  
269 and summer driven by vapor diffusion into the subsoil. While the rate is small (it can hardly be seen in Figure 3a, so we  
270 zoom it in Figure 4), it occurs throughout the late spring and summer, after the subsoil has started to thaw. Overall, it is  
271 about half of recharge from direct rainfall infiltration, but much more regular (it occurs every year) and quite robust, in that it  
272 displays little sensitivity to model results(See Table 2).

273 Vapor diffusion between the surface and subsoil layers is positive (downwards) during spring and early summer, because  
274 then the temperature and, therefore, vapor pressure is higher in the surface than in the subsoil. The flux fluctuates during late  
275 winter, when the subsoil has started to warm, so that vapor diffuses upwards during cold days and downwards during warm  
276 days. Diffusion is consistently upwards during autumn and winter, but the rate is very low because the saturated vapor  
277 pressure is low and changes little with temperature (that is,  $dp_{v,sat}/dT$  is small) at low temperatures. Therefore, there is a net  
278 downward vapor flux. Its amount is not very large, but as mentioned above, it is what drives recharge during spring and early  
279 summer.



280  
 281 **Figure 3.** Daily evolution of (a) precipitation and recharge, (b) other water fluxes, (c) water content at surface (solid line)  
 282 and subsoil (dashed line), (d, e) heat fluxes, and (f) temperatures of the base model



283

284 **Figure 4.** Zoom of recharge (red dashed line) and vapor diffusion (blue line) during 2003 (Temperatures are also shown).

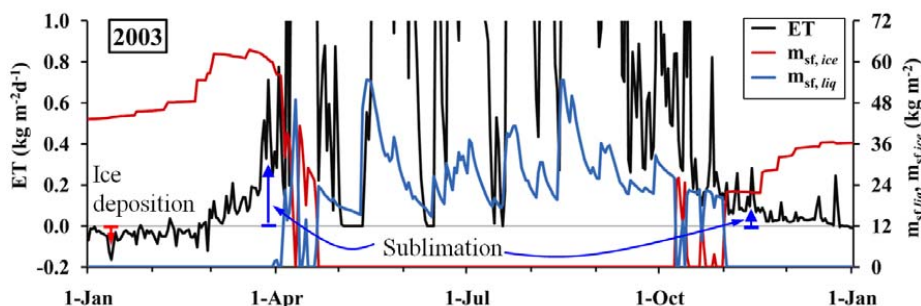
285 Note that, except for the two heavy rainfall events of May and August, recharge during the warming period (after the subsoil

286 has started to thaw) is identical to the vapor diffusion flux.

287 Vapor diffusion is basically controlled by the diffusion coefficient ( $D$ ), which is the only parameter that affects the vapor  
 288 diffusion flux significantly (Table 2). Reducing  $D$  leads obviously to a reduction of vapor diffusion. A similar effect results  
 289 from increasing the soil surface thickness, which results in an apparent reduction of the gradient. As less water is transported  
 290 downwards, evapotranspiration increases and recharge decreases.

291 As expected, evapotranspiration is the main sink of water. In fact, it is limited by water availability during the warm season,  
 292 being high only after rainfall events and during melting (Figure 3.b). The evapotranspiration is about 85% of rainfall (Table  
 293 2), which is similar to the results obtained by Ma et al., (2003) for the Selenge River basin, northern Mongolia. Note that the  
 294 evapotranspiration is very small during winter because low temperatures hinder vaporization. In fact, it is negative (i.e., ice  
 295 deposition) during January and February (Figure 5), when the soil is colder than the air. Sublimation only becomes relevant  
 296 in March. Cumulative sublimation (some  $29 \text{ kg m}^{-2} \text{ year}^{-1}$  in 2003) is low compared to typical values of cold regions (see,  
 297 e.g., Zhou et al., 2014), but large compared to winter rainfall.

298 The whole cycle is driven by radiation, which follows the usual seasonal patterns, high during late spring and early summer  
 299 and low in winter, when net radiation may become negative, partly due to the high albedo of snow (Figure 3.d). The  
 300 radiation balance is highly sensitive to orientation of the slope (Table 3). Obviously, the south face receives more radiation  
 301 than the north face. But this is largely compensated by an increase in sensible heat flux. The sensible heat increases when  
 302 latent heat decreases. That is, heat is returned to the atmosphere either as latent heat when water is available for evaporation,  
 303 or as sensible heat when the soil is dry. According to the energy balance (Table 3), the sensible heat is higher than the latent  
 304 heat flux, which reflects the dry climate of region. As a result the effect of slope and orientation is smaller than we had  
 305 anticipated (Tables 2 and 3). The large increase in radiation of south facing slopes only results in a small increase in  
 306 evaporation and latent heat and a parallel reduction of infiltration and recharge decreases (Table 2), because there is little  
 307 water.



308  
 309 **Figure 5.** Zoom of ET (actually, water phase change processes) (black line) along with liquid (blue) and ice (red) water  
 310 contents during 2003.

311 The dependence of the two balances on slope is non-monotonic, which points to the complexity of the system, even in the  
 312 relatively simple model we are presenting here. Radiation is dramatically reduced in north facing slopes, which causes a  
 313 reduction in ET, but the reduction is very small as discussed above, and not sufficient to cause an increase in infiltration. The  
 314 reduction in ET is compensated by an increase in surface runoff and latent heat diffusion (vapor convection) downwards.  
 315 The non-monotonic dependence of vapor convection on slope also illustrates the robustness of vapor diffusion. It is slightly  
 316 larger in south facing slopes than in horizontal land because surface temperatures are also larger. But it is also slightly larger  
 317 in north facing slopes than in horizontal land because subsoil temperatures are lower.

318 **Table 2.** Average in 5 years of water fluxes: evapotranspiration (ET), infiltration (I), surface runoff (SR), vapor diffusion  
 319 ( $J_D$ ) and Recharge (R). Precipitation is  $334 \text{ kg m}^{-2} \text{ year}^{-1}$

Water Bal. [ $\text{kg m}^{-2} \text{ year}^{-1}$ ]	ET	I	SR	$J_D$	R
Base model	284.9	30.9	0.1	18.1	48.8
South face	290.8	23.8	0.0	19.5	43.3
North face	283.8	30.2	1.0	19.0	49.1
$z_0$ (x 2)	289.8	26.8	0.0	17.5	44.1
$\epsilon_s$ (0.94 $\rightarrow$ 0.99)	280.6	35.5	1.0	16.9	52.2
$K_{\text{sat}}$ (x 0.1)	288.2	12.8	14.9	18.1	30.6
$\theta^{\text{WP}}$ (x 2)	252.9	66.0	2.1	13.1	79.1
D (x 0.25)	296.1	32.6	0.0	5.3	37.8
$L_{\text{sf}}$ (x 2)	318.5	4.2	0.0	11.4	15.6
$L_{\text{ss}}$ (1.5 $\rightarrow$ 2.15)	267.9	30.2	0.0	36.0	66.2

320





321 The limited availability of water causes most rainfall to evaporate. It also implies a low sensitivity of ET parameters to water  
 322 and energy fluxes. For example, increasing roughness length ( $z_0$ ) decreases the aerodynamic resistance ( $r_a$ ), which leads to  
 323 small increases in both latent and sensible heat fluxes and a parallel small decrease in infiltration and recharge. Similarly,  
 324 increasing land surface emissivity from 0.94 to 0.99 reduces considerably net radiation as more longwave radiation is  
 325 emitted, but is compensated by a decrease of sensible and, to a lesser extent, latent heat fluxes.

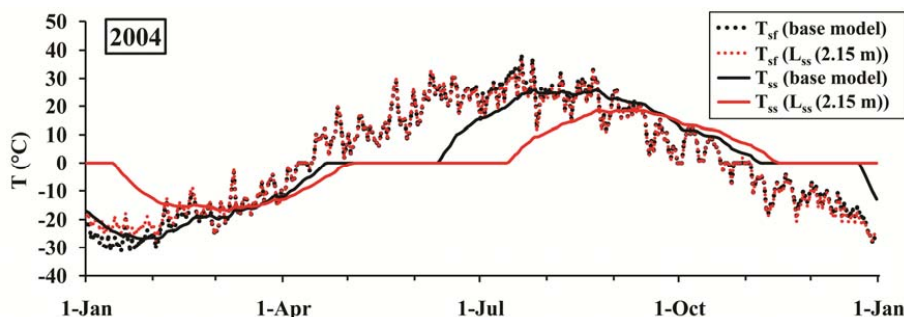
326 **Table 3.** Average in 5 years of energy fluxes: net radiation (Rn), Latent heat ( $e_g ET$ ), sensible heat (H), heat conduction (G)  
 327 and vapor convection ( $e_g J_D$ ).

Energy Bal. [ $MJ\ m^{-2}\ year^{-1}$ ]	Rn	$e_g ET$	H	G	$e_g J_D$
Base model	2064.4	717.1	1345.6	-45.8	45.9
South face	2610.7	732.3	1876.8	-49.1	49.4
North face	1708.4	714.6	992.3	-48.0	48.1
$z_0$ (x 2)	2181.4	729.5	1450.5	-44.2	44.3
$\epsilon_s$ (0.94 → 0.99)	1739.1	706.4	1030.9	-42.9	42.9
$K_{sat}$ (x 0.1)	2067.2	725.4	1340.1	-45.4	45.9
$\theta^{WP}$ (x 2)	2041.5	636.6	1402.1	-34.4	33.1
D (x 0.25)	2072.4	745.5	1325.8	-14.3	13.6
$L_{sf}$ (x 2)	1980.5	801.8	1177.9	-28.6	29.0
$L_{ss}$ (1.5 → 2.15)	2032.0	675.2	1355.5	-91.4	91.1

328

329 The most surprising energy balance terms are heat conduction (soil heat flux) and vapor convection (Figure 3.e). Conductive  
 330 heat flux is usually considered seasonal, with yearly averages close to zero. Downward heat fluxes in summer are usually  
 331 balanced by upward fluxes in winter (e.g. Alkhaier et al., 2012). In our case, even though the subsoil remains frozen for long  
 332 (more than 7 months, compared to less than six the surface layer), there is a net flux upwards, to compensate the latent heat  
 333 convection associated to vapor diffusion, which is downwards, as was discussed before. Therefore, it is not surprising that all  
 334 factors that reduce the soil heat flux cause an increase in vapor convection, and vice versa.

335 The temperature oscillates more at the surface than at the subsoil layer (Figure 3.f). The differences of temperature of the  
 336 layers are higher in summer. One can observe clearly the periods of melting and freezing of the subsoil layer with  
 337 temperatures of  $0^\circ C$ . The annual average surface layer temperature was  $0.8^\circ C$  for 2003 and  $2.0^\circ C$  for 2004 while the air  
 338 temperature was  $-3.6^\circ C$  for 2003 and  $-2.4^\circ C$  for 2004. For subsoil layer,  $-0.5^\circ C$  and  $0.7^\circ C$ , in 2003 and in 2004 respectively.  
 339 An increase of the subsoil length ( $L_{ss}$ ) leads to temperatures in the subsoil that oscillate less due to the increased heat storage  
 340 capacity. This leads to larger temperature differences between surface and subsoil, which according to our model (equation  
 341 9, Figure 6) leads to larger vapor diffusion. As more water is transported downwards, evapotranspiration decreases and  
 342 recharge increases.



343  
344

Figure 6. Daily evolution of surface and subsoil temperature in 2004.

#### 345 4. Discussion and Conclusions

346 We have developed a water and energy balance model that contains two layers and attempts to represent all terms relevant  
347 for simulating land surface hydrological processes, including all possible phase changes and, singularly, vapor diffusion. The  
348 model has been applied using meteorological data from the Terej station, northern Mongolia and typical soil properties of  
349 the region. Results are consistent with local observations by others:

- 350 - Direct surface runoff is negligible and restricted to snowmelt periods.
- 351 - Liquid infiltration and subsequent recharge are restricted to a few heavy rainfall events. However, a sizable  
352 recharge (about half of that from rainfall events) occurs continuously during late spring and early summer.
- 353 - Evapotranspiration is limited by water availability, as it accounts for 85% of rainfall. Sublimation is restricted to  
354 late fall and spring, but it is also large, compared to winter snowfall. Ice deposition occurs most days during January  
355 and February.
- 356 - Sensible heat is higher than latent heat flux, which reflects the dry climate of the region and low precipitation.
- 357 - The active layer remains frozen during the winter with periods of freezing or thawing of some three months, a  
358 length of time that increases when the thickness of the active layer increases.

359 In summary, results are qualitatively consistent with observations. Notably, total runoff would be too small, compared to  
360 observations, if vapor diffusion is reduced. The most singular result of the simulations is the relative importance of vapor  
361 diffusion, which is downwards during spring and early summer, when temperature and, therefore, vapor pressure are higher  
362 in the surface than in the subsoil. The upwards vapor diffusion flux is much smaller than the downward one, because vapor  
363 pressure is a non-linear function of temperature. This downward flux transforms into recharge, which is continuous, although  
364 fluctuating during that period.

365 In summary, the net downward vapor flux is relevant both in terms of water balance, accounting for a sizable portion of  
366 recharge, and energy balance, causing a net upwards flux of heat. We conclude that land surface schemes should account for  
367 vapor diffusion. We notice that, being a diffusive process, it may be included in such schemes at a moderate effort. Still,



368 further research is needed to ascertain the right values of diffusion coefficient to be used and the way of discretizing Fick's  
 369 Law, that is, the choice of length over which diffusion takes place in equation (9).

## 370 Appendix A

### 371 Position of the sun

372 For the calculation of the position of the sun and the zenith, it is convenient to define two unit vectors:  $\mathbf{p}$ , which is  
 373 orthogonal to the land surface and  $\mathbf{s}$ , which points to the sun (Figure A1). Their first component points eastwards, the second  
 374 northwards and the third upwards. Vector  $\mathbf{p}$  can be calculated from the strike ( $\sigma$ ) and dip ( $\theta$ ) (see also figure A2):

$$\mathbf{p} = \begin{pmatrix} p_{east} \\ p_{north} \\ p_{up} \end{pmatrix} = \begin{pmatrix} \cos \sigma \sin \theta \\ -\sin \sigma \sin \theta \\ \cos \theta \end{pmatrix} \quad (\text{A1})$$

375 Vector  $\mathbf{s}$  depends on the time of the day, the sun declination ( $\delta$ ), solar angle ( $\omega$ ) and the latitude ( $\varphi$ ). It can be calculated  
 376 according to Sproul (2007) as:

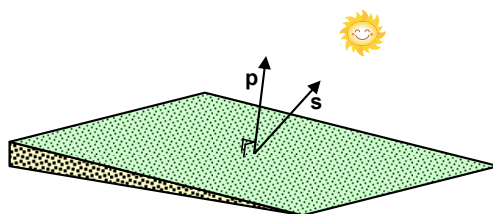
$$\mathbf{s} = \begin{pmatrix} s_{east} \\ s_{north} \\ s_{up} \end{pmatrix} = \begin{pmatrix} -\cos \delta \sin \omega \\ \sin \delta \sin \varphi - \cos \delta \sin \varphi \cos \omega \\ \cos \delta \cos \varphi \cos \omega + \sin \delta \sin \varphi \end{pmatrix} \quad (\text{A2})$$

377 The product of both vectors ( $\mathbf{p}^T \mathbf{s}$ ) equals the cosine of the angle between them. Note, that on a horizontal surface ( $\theta = 0$ ),  $\mathbf{p}^T$   
 378 is (0,0,1) and  $\mathbf{p}^T \mathbf{s} = s_{up}$ . At night  $s_{up} < 0$ , at daylight  $s_{up} > 0$  and at sunrise and sunset  $s_{up} = 0$ . Furthermore, an inclined  
 379 surface is in the shade when  $\mathbf{p}^T \mathbf{s} < 0$ .

380 The sun declination ( $\delta$ ) is the angle between the direction of the sun and the equator. It can be calculated by a yearly  
 381 sinusoidal function:

$$\delta = -\delta_{max} \sin \left( 2\pi \frac{t - t_s}{d_a} \right) \quad (\text{A3})$$

382 where  $\delta_{max}$  is the maximum sun declination (0.4091 rad = 23.26°),  $t$  is time (s),  $t_s$  is time at September equinox,  
 383 approximately September 21<sup>st</sup>, (s) and  $d_a$  is the duration of year (=365.241 days = 3.15568 × 10<sup>7</sup>s).



384  
 385

Figure A1. Illustration of vectors  $\mathbf{p}$  and  $\mathbf{s}$



386 The extraterrestrial solar radiation on a horizontal surface can be simplified by:

$$R_{S,et,hor} = S_0 f_e s_{up} = S_0 f_e (\cos \delta \cos \varphi \cos \omega + \sin \delta \sin \varphi) \quad \text{If } s_{up} > 0$$

$$R_{S,et,hor} = 0 \quad \text{otherwise} \quad (A4)$$

387 where  $S_0$  is the sun constant ( $1367 \text{ J m}^{-2} \text{ s}^{-1}$ ) and  $f_e$  is the factor that corrects for the eccentricity of the earth's orbit. It can be  
 388 calculated from (Allen et al., 1998):

$$f_e = 1 + 0.033 \cos\left(2\pi \frac{t - t_{ph}}{d_a}\right) \quad (A5)$$

389 where  $t_{ph}$  is the time at perihelion, approximately January 3<sup>rd</sup>, (s).

390 For the daily averaged extraterrestrial solar radiation on a horizontal surface, integrating equation (A4) between sunset and  
 391 sunrise and dividing by the duration of a day ( $d_d$ ) gives:

$$R_{S,et,hor} = \frac{S_0 f_e}{d_d} \int_{-\omega_{ss}}^{\omega_{ss}} s_{up} dt = \frac{S_0 f_e}{d_d} (\cos \delta \cos \varphi \sin \omega_{ss} + \omega_{ss} \sin \delta \sin \varphi) \quad (A6)$$

392 where the sunset angle,  $\omega_{ss}$ , is the solar angle when  $s_{up}$  equals 0:

$$\omega_{ss} = \cos^{-1} (\max (\min (-\tan \varphi \tan \delta, 1), -1)) \quad (A7)$$

393 The min and max functions guarantee that  $\omega_{ss} \in [0, \pi]$ . Thus, equation (A6) also works for days when the sun doesn't set or  
 394 rise (i.e., in polar regions).

### 395 Correction for an inclined surface

396 The strike ( $\sigma$ ) of an inclined plane is the orientation of a horizontal line on this plane, expressed as an angle relative to the  
 397 north in clockwise direction. The dip ( $\theta$ ) is the maximum angle between a horizontal plane and the incline plane (figure A2).

398 The extraterrestrial solar radiation on an inclined surface is the solar radiation without taking into account the reduction of it  
 399 by the atmosphere. It can be expressed as:

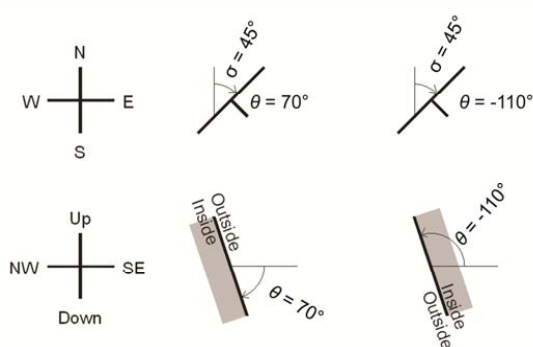
$$R_{S,et,inc} = S_0 f_e \max(\mathbf{p}^T \mathbf{s}, 0) \quad \text{If } s_{up} > 0$$

$$R_{S,et,inc} = 0 \quad \text{otherwise} \quad (A8)$$

400 Note that for a horizontal surface ( $\theta = 0 \Rightarrow \mathbf{p}^T \mathbf{s} = s_{up}$ ) equation (A8) reduces to (A4). For the daily averaged extraterrestrial  
 401 solar radiation on an inclined surface, we have to integrate equation (A8):

$$R_{S,et,inc} = \frac{S_0 f_e}{d_d} \int_{-\omega_{ss}}^{\omega_{ss}} \max(\mathbf{p}^T \mathbf{s}, 0) dt \quad (A9)$$

402



403

404 **Figure A2.** Illustration of strike ( $\sigma$ ) and dip ( $\theta$ ). Note that a dip between  $-0.5\pi$  and  $0.5\pi$  ( $-90^\circ$  and  $90^\circ$ ) refers to a plane with  
 405 its outside facing upwards. A dip between  $1.5\pi$  and  $0.5\pi$  ( $90^\circ$  and  $270^\circ$ ) or between  $-1.5\pi$  and  $-0.5\pi$  refers to a plane with its  
 406 outside facing downwards.

407 However, we have to take into account that the surface can be in the shade during part of the day, which complicates the  
 408 calculations. The integral of  $\max(\mathbf{p}^T \mathbf{s}, 0)$  can be calculated by dividing it into different periods, when it is in the shade or  
 409 not:

$$\int_{-\omega_{ss}}^{\omega_{ss}} \max(\mathbf{p}^T \mathbf{s}, 0) dt = \max\left(\int_{-\omega_{ss}}^{\omega_1} \mathbf{p}^T \mathbf{s} dt, 0\right) + \max\left(\int_{\omega_1}^{\omega_2} \mathbf{p}^T \mathbf{s} dt, 0\right) + \max\left(\int_{\omega_2}^{\omega_{ss}} \mathbf{p}^T \mathbf{s} dt, 0\right) \quad (\text{A10})$$

$$\omega_1 = \min(\max(-\omega_{ss}, \omega_{i01}), \omega_{ss})$$

$$\omega_2 = \min(\max(-\omega_1, \omega_{i02}), \omega_{ss})$$

410 where  $\omega_{i01}$  and  $\omega_{i02}$  are the two solar angles in a day when the inclined surface comes out of or into the shade, that is, when  
 411  $\mathbf{p}^T \mathbf{s} = 0$ . They are calculated from:



if  $-1 \geq \frac{b}{a\sqrt{1+b^2/a^2}} \geq 1$  and  $-1 \geq \frac{c}{a\sqrt{1+b^2/a^2}} \geq 1$  then

$$\omega_{io1} = \min(\text{mod}(\pi - \omega_b + \omega_c, 2\pi) - \pi, \text{mod}(-\omega_b - \omega_c, 2\pi) - \pi)$$

$$\omega_{io2} = \max(\text{mod}(\pi - \omega_b + \omega_c, 2\pi) - \pi, \text{mod}(-\omega_b - \omega_c, 2\pi) - \pi)$$

$$\omega_b = \frac{b}{a\sqrt{1+b^2/a^2}} \tag{A11}$$

$$\omega_c = \frac{c}{a\sqrt{1+b^2/a^2}}$$

else (there is no solution for  $\mathbf{p}^T \mathbf{s} = 0$ )

$$\omega_{io1} = -\pi$$

$$\omega_{io2} = \pi$$

412 where mod is a function that returns the remainder of the first argument after it is divided by the second argument. This  
 413 guarantees that  $\omega_1$  and  $\omega_2 \in [-\pi, \pi]$ . Moreover, the min and max functions guarantee that  $\omega_{io1} \leq \omega_{io2}$ . When there is no  
 414 solution for  $\mathbf{p}^T \mathbf{s} = 0$ , it means that during the whole day the inclined surface is facing the sun or not. The integral of  $\mathbf{p}^T \mathbf{s}$  can  
 415 be calculated by using equations (A1) and (A2):

$$\begin{aligned} \int_{\omega_{ini}}^{\omega_{fin}} \mathbf{p}^T \mathbf{s} dt &= \int_{\omega_{ini}}^{\omega_{fin}} (a \sin \omega + b \cos \omega - c) dt = \\ &= \frac{d_d}{2\pi} [-a(\cos \omega_{fin} - \cos \omega_{ini}) + b(\sin \omega_{fin} - \sin \omega_{ini}) - c(\omega_{fin} - \omega_{ini})] \end{aligned} \tag{A12}$$

416 with

$$a = -\cos \sigma \sin \theta \cos \delta$$

$$b = \sin \sigma \sin \theta \cos \delta \sin \varphi + \cos \theta \cos \delta \cos \varphi \tag{A13}$$

$$c = \sin \sigma \sin \theta \sin \delta \cos \varphi - \cos \theta \sin \delta \sin \varphi$$

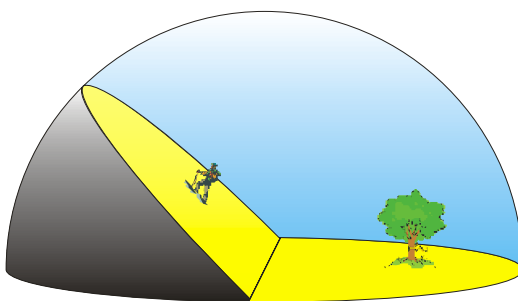
417 *Sky view factor*



418 The sky view factor ( $f_{sv}$ ), is the proportion of the sky above the inclined surface that is not blocked from view by the  
419 surrounding horizontal plane (figure A3). It ranges from 0.5 for a vertical to 1 for a horizontal surface. In general one can use  
420 the formula of Badescu (2002):

$$f_{sv} = \frac{\cos(2\theta) + 2}{4} \quad (\text{A14})$$

421



422

423

**Figure A3.** Illustration of the sky view factor,  $f_{sv}$ .

424

## 425 Appendix B

426

427 To test the validity of the discrete approximation of the diffusive vapor flux, we simulate the experiments of Gran et al  
428 (2011a and b). Because of differences in the setting (Gran's experiments were performed in the laboratory), we had to do  
429 several changes in the spreadsheet. These are highlighted in yellow in the spreadsheet, also available in the website together  
430 with the original general use spreadsheet, and we discuss them here.

431 Meteorological data had to be changed. There is no rainfall, we assumed zero wind velocity and the net radiation was fixed  
432 at  $750 \text{ W m}^{-2}$ , value reported by Gran et al., (2011a).

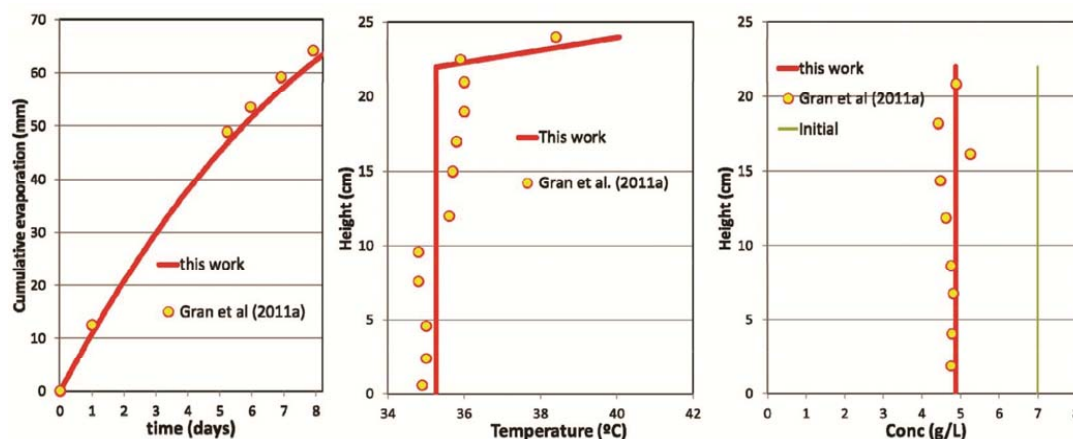
433 Since the experimental column loses heat through the column sides, we had to add a sensible heat sink of the form  $\alpha(T_{env} -$   
434  $T_{cot})$  in both the subsoil (ss) and soil surface (sf) layers. When we adopted the value reported by Gran et al. (2011b) for  $\alpha$ ,  
435 the column cooled down too much. In examining her input files, we realized the value she reports in the paper is not correct.  
436 The right value is far smaller.

437 The column thickness is 24 cm. So, we adopted a thickness of 2 cm for the top layer and 22 for the bottom.

438 As the thickness is small, capillary fluxes are relevant. We computed them as proportional to the difference in water content,  
439 and adjusted the proportionality constant so as to fit observations (Figure B1)



440 The initial calculations (with large  $\alpha$  for lateral heat exchange, see above) were unstable, so we had to reduce the time step  
441 from 1 day to 1 hour, which was also a test of the internal consistency of the spreadsheet. As it turned out, results would  
442 have also been stable with the final reduced  $\alpha$ , but we still kept the 1 h time step.  
443 As shown in Figure B1, results are quite good (note that no diffusion or boundary layer parameters were touched from those  
444 of the basic spreadsheet). So we left it at that, without trying to perform a formal calibration (an informal trial and error  
445 calibration was effectively performed when adjusting the lateral heat exchange and the capillary flux).  
446



447  
448 **Figure B1.** Time evolution of cumulative evaporation (left), spatial distribution of Temperature (center) and concentration  
449 (right) at the end of the experiment of Gran et al. (2011a).  
450

#### 451 References

452 Alkhaier, F., Su, Z. and Flerchinger, G.N.: Reconnoitering the effect of shallow groundwater on land surface temperature  
453 and surface energy balance using MODIS and SEBS, *Hydrology and Earth System Sciences.*, 16(7), 1833-1844, 2012.  
454 Allen, R.G., Pereira, L.S., Raes, D. and Smith, M.: Crop evapotranspiration-Guidelines for computing crop water  
455 requirements-FAO Irrigation and drainage paper 56, FAO, Rome., 300(9), D05109, 1998.  
456 Allen, R. G., Trezza, R. and Tasumi, M.: Analytical integrated functions for daily solar radiation on slopes, *Agricultural and*  
457 *Forest Meteorology.*, 139(1), 55-73, 2006.  
458 Arnold J.G., Srinivasan, R., Muttiah, R.S. and Williams, J.R.: Large area hydrological modeling and assessment, part I:  
459 Model development, *Journal of the American Water Resources Association.*,34(1), 73-89, 1998.  
460 Arya, S.P.: Introduction to Micrometeorology, Academic Press, 420 pp,2001.





- 461 Asner, G.P., Scurlock, J.M. and Hicke, J.A.: Global synthesis of leaf area index observations: implications for ecological and  
462 remote sensing studies, *Global Ecology and Biogeography*, 12(3), 191-205, 2003.
- 463 Badescu, V.: 3D isotropic approximation for solar diffuse irradiance on tilted surfaces, *Renewable Energy*, 26, 221-233,  
464 2002.
- 465 Blad, B.L. and Rosenberg, N.J.: Evaluation of Resistance and Mass Transport Evapotranspiration Models Requiring Canopy  
466 Temperature Data, *Agron. J.*, 68, 764–769, 1976.
- 467 Boland, J., Ridleya, B. and Brown, B.: Models of diffuse solar radiation, *Renewable Energy*, 33, 575-584, 2008.
- 468 Bristow, K.L.: Thermal Conductivity, *Methods of Soil Analysis: Part 4 Physical Methods*, 1209-1226, 2002.
- 469 Brutsaert, W.: On a derivable formula for long-wave radiation from clear skies. *Water Resources Research*, 11(5), 742-744,  
470 1975.
- 471 Brutsaert, W.: *Evaporation into the Atmosphere*, R. Deidel Publishing Company, Dordrecht, Holland, 1982.
- 472 Cass, A., Campbell, G. S. and Jones, T. L.: Enhancement of thermal water vapor diffusion in soil, *Soil Science Society of  
473 America Journal*, 48(1), 25-32, 1984.
- 474 Côté, J. and Konrad, J.M.: A generalized thermal conductivity model for soils and construction materials, *Canadian  
475 Geotechnical Journal*, 42(2), 443-458, 2005.
- 476 Cussler, E. L.: *Diffusion: Mass Transfer in Fluid Systems*, Cambridge University Press, New York, 1997.
- 477 Dandar, E., Carrera, J. and Nemer, B.: Evaluation of groundwater resources in the upper Tuul River basin, Mongolia, *Water  
478 and Environment in the Selenga-Baikal Basin: International Research Cooperation for an Eco region of Global  
479 Relevance*, Columbia University Press, 2016.
- 480 Dulamsuren, C., Hauck, M., Bader, M., Osokhjargal, D., Oyungerel, S., Nyambayar, S. and Leuschner, C.: Water relations  
481 and photosynthetic performance in *Larix sibirica* growing in the forest-steppe ecotone of northern Mongolia, *Tree  
482 physiology*, 29(1), 99-110, 2008.
- 483 Evett, S.R., Prueger, J.H. and Tolk, J.A.: Water and energy balances in the soil-plant-atmosphere continuum, *Handbook of  
484 Soil Sciences: Properties and Processes*, 6-1, 2011.
- 485 Flerchinger, G.N.: *The Simultaneous Heat and Water (SHAW) Model: Technical Documentation, Version 3.0. Technical  
486 Report NWRC 2017-02, Northwest Watershed Research Center, USDA, Agricultural Research Service Boise, Idaho,  
487 2017.*
- 488 Fuka, D.R., Easton, Z.M., Brooks, E.S., Boll, J., Steenhuis, T.S. and Walter, M.T.: A simple process-based snowmelt routine  
489 to model spatially distributed snow depth and snowmelt in the SWAT model, *Journal of the American Water Resources  
490 Association*, 48(6), 1151-1161, 2012.
- 491 Gran, M., Carrera, J., Massana, J., Saaltink, M. W., Olivella, S., Ayora, C. and Lloret, A.: Dynamics of water vapor flux and  
492 water separation processes during evaporation from a salty dry soil. *Journal of hydrology*, 396(3), 215-220, 2011a.
- 493 Gran, M., Carrera, J., Olivella, S. and Saaltink, M. W.: Modeling evaporation processes in a saline soil from saturation to  
494 oven dry conditions, *Hydrology and Earth System Sciences*, 15(7), 2077-2089, 2011b.



- 495 Gravis, G.F., Gavrilova, M.K., Zabolotnik, S.I., Lisun, A.M., Suhodrovsky, V.L. and Tumurbaatar, L.: Geocryological  
496 conditions in Mongolia, Yakutsk, Russia, 1972. (in Russian).
- 497 Gusev, Y. M. and Nasonova, O. N.: The simulation of heat and water exchange at the land–atmosphere interface for the  
498 boreal grassland by the land surface model SWAP, *Hydrological processes.*, 16(10), 1893-1919, 2002.
- 499 Haddeland, I., D.B. Clark, W. Franssen, F. Ludwig, F. Voss, N.W. Arnell, N. Bertrand, M. Best, S. Folwell, D. Gerten, S.  
500 Gomes, S.N. Gosling, S. Hagemann, N. Hanasaki, R. Harding, J. Heinke, P. Kabat, S. Koirala, T. Oki, J. Polcher, T.  
501 Stacke, P. Viterbo, G.P. Weedon, and P. Yeh: Multimodel Estimate of the Global Terrestrial Water Balance: Setup and  
502 First Results, *Journal of Hydrometeorology*, 12(5), 869-884, 2011.
- 503 Hanasaki, N., Kanae, S., Oki, T., Masuda, K., Motoya, K., Shen, Y. and Tanaka, K.: An integrated model for the assessment  
504 of global water resources? Part 1: Input meteorological forcing and natural hydrological cycle modules, *Hydrology and*  
505 *Earth System Sciences.*, 12, 1007-1025, 2008.
- 506 Hargreaves, G.H. and Samani, Z.A.: Reference crop evapotranspiration from air temperature, *Applied engineering in*  
507 *agriculture.*, 1(2), 96-99, 1985.
- 508 Hargreaves, G.H. and Allen, R.G.: History and Evaluation of Hargreaves Evapotranspiration Equation, *Journal of Irrigation*  
509 *and Drainage Engineering.*, 129(1), 53-63. doi: 10.1061(ASCE)0733-9437(2003)129:1(53), 2003.
- 510 Herrero, J. and Polo, M. J.: Parameterization of atmospheric longwave emissivity in a mountainous site for all sky  
511 conditions, *Hydrol. Earth Syst. Sci.*, 16, 3139–3147, doi:10.5194/hess-16-3139- 2012, 2012.
- 512 Hülsmann, L., Geyer, T., Schweitzer, C., Priess, J. and Karthe, D.: The effect of subarctic conditions on water resources:  
513 initial results and limitations of the swat model applied to the Kharaa river basin in Northern Mongolia, *Environmental*  
514 *Earth Sciences.*, 73(2), 581-592, 2015.
- 515 Ishikawa, M., Sharkhuu, N., Zhang, Y., Kadota, T. and Ohata, T.: Ground thermal and moisture conditions at the southern  
516 boundary of discontinuous permafrost, Mongolia, *Permafrost and Periglacial Processes.*, 16(2), 209-216, 2005.
- 517 Jambaljav, Ya., Dashtseren, A., Solongo, D., Saruulzaya, D. and Battogtokh, D.: The temperature regime in boreholes at  
518 Nalaikh and Terej sites in Mongolia, *Proceedings of the Ninth International Conference on Permafrost.*, University of  
519 Alaska, Fairbanks, Volume 1, pp. 821-825, 2008.
- 520 Jansson, P-E. and Moon, D.S., 2001: A coupled model of water, heat and mass transfer using object orientation to improve  
521 flexibility and functionality. *Environmental Modelling and Software*, 16:37-46
- 522 Katul, G.G. and Parlange, M.B.: A Penman-Brutsaert Model for wet surface evaporation, *Water Resources Research.*, 28(1),  
523 121-126, 1992.
- 524 Ma, X., Yasunari, T., Ohata, T., Natsagdorj, L., Davaa, G. and Oyumbaatar, D.: Hydrological regime analysis of the Selenge  
525 River basin, Mongolia, *Hydrological Processes.*, 17(14), 2929-2945, 2003.
- 526 McKenzie, J. M. and C.I Voss: Permafrost thaw in a nested groundwater-flow system. *Hydrogeol J*, 21(1), 299-316, 2013.
- 527 McMahon, T.A., Peel, M.C., Lowe, L., Srikanthan, R. and McVicar, T.R.: Estimating actual, potential, reference crop and  
528 pan evaporation using standard meteorological data: a pragmatic synthesis, *Hydrology and Earth System*  
529 *Sciences.*, 17(4), 1331-1363, 2013.



- 530 Monteith, J.L. and Unsworth, M.H.: Principles of Environmental Physics, Academic Press, 291 pp, 1990.
- 531 Murray, F.W.: On the computation of saturation vapor pressure, *J. Appl. Meteor.*, 6, 203–204, 1967.
- 532 National soil atlas of Mongolia. (1981) (Scale 1:1000 000)
- 533 Noorian, A. M., Moradi, I. and Kamali, G. A.: Evaluation of 12 models to estimate hourly diffuse irradiation on inclined  
534 surfaces, *Renewable energy.*, 33(6), 1406-1412, 2008.
- 535 Oke, T.R.: Boundary Layer Climates, 2nd edition, Halsted, New York, 1987.
- 536 Olivella, S., Gens, A., Carrera, J. and Alonso, E.E.: Numerical formulation for a simulator (code `bright`) for the coupled  
537 analysis of saline media. *Eng. Comput.* 13(7), 87–112, 1996. doi: 10.1108/02644409610151575
- 538 Penman, H.L.: Natural evaporation from open water, bare soil and grass, In *Proceedings of the Royal Society of London A:*  
539 *Mathematical, Physical and Engineering Sciences.*, Vol.193, 120-145, 1948.
- 540 Priestley, C.H.B. and Taylor, R.J.: On the assessment of surface heat flux and evaporation using large scale parameters,  
541 *Mon. Weather Rev.*, 100, 81-92, 1972.
- 542 Ripple, C.D., Rubin, J. and Van Hylckama, T.E.A.: Estimating Steady-state Evaporation Rates from bare Soils under  
543 Conditions of High Water Table, U.S. Geol. Sur., Open-file Report Water Res. Div., Menlo Park, California, 62 pp,  
544 1970.
- 545 Rosenberg, N.J., Blad, B.L. and Verma, S.B.: Evaporation and Evapotranspiration, Chapter7 of the Book *Microclimate –*  
546 *The Biological Environment*, Wiley-Interscience, John Wiley and Sons, 209–287, 1983.
- 547 Saito, H. and Šimůnek, J.: Effects of meteorological models on the solution of the surface energy balance and soil  
548 temperature variations in bare soils, *Journal of Hydrology.*, 373(3), 545-561, 2009.
- 549 Schroeder, P.R., Dozier, T.S., Zappi, P.A., McEnroe, B.M., Sjostrom, J.W. and Peyton, R.L.: The hydrologic evaluation of  
550 landfill performance (HELP) model: engineering documentation for version 3, Environmental Protection Agency, United  
551 States., 1994.
- 552 Sharkhuu, N.: Recent changes in the permafrost of Mongolia, In *Proceedings of the 8th International Conference on*  
553 *Permafrost.*, Zurich, Switzerland, pp.1029/1034, 2003.
- 554 Shuttleworth, W. J.: Evaporation, Institute of Hydrology, Wallingford, 1979.
- 555 Shvetzov, P.F.: Conditions and geothermal consequences of the moisture exchange between the lithosphere and the  
556 atmosphere in permafrost regions, *Third international conference on permafrost.*, Ottawa, Ontario, 1978.
- 557 Sicart, J.E., Pomeroy, J.W., Essery R.L.H. and Bewley, D.: Incoming longwave radiation to melting snow: observations,  
558 sensitivity and estimation in northern environments, *Hydrol.Processes.*, 20, 3697-3708, doi: 10.1002/hyp.6383, 2006.
- 559 Šimůnek, J., M. Th. van Genuchten, and M. Šejna. 2008. Development and Applications of the HYDRUS and STANMOD  
560 Software Packages and Related Codes. *Vadose Zone J.* 7:587-600. doi:10.2136/vzj2007.0077
- 561 Sproul, A.B.: Derivation of the solar geometric relationships using vector analysis, *Renewable Energy.*, 32(7), 1187-1205,  
562 doi: 10.1016/j.renene.2006.05.001, 2007.
- 563 Tian, Y.Q., Davies-Colley, R.J., Gong, P. and Thorrold, B.W.: Estimating solar radiation on slopes of arbitrary aspect,  
564 *Agricultural and Forest Meteorology.*, 109, 67-74, 2001.



- 565 Tuvshinjargal, D. and Saranbaatar, L.: Thermal balance features in the Terelj valley (Mongolia), In proceedings of the 3rd  
566 International Workshop on Terrestrial Change in Mongolia., Tsukuba, Japan, 2004.
- 567 Qi, J., Li, S., Li, Q., Xing, Z., Bourque, C.P.A. and Meng, F.R.: A new soil-temperature module for SWAT application in  
568 regions with seasonal snow cover, *Journal of Hydrology.*, 538, 863–877, doi: 10.1016/j.jhydrol.2016.05.003, 2016.
- 569 Xu, C.Y. and Singh, V.P.: Cross comparison of empirical equations for calculating potential evapotranspiration with data  
570 from Switzerland, *Water Resources Management.*, 16(3), 197-219, 2002.
- 571 Yates, D.N.: WatBal: An Integrated Water Balance Model for Climate Impact Assessment of River Basin Runoff,  
572 *International Journal of Water Resources Development.*, 12(2), 121-140, doi: 10.1080/07900629650041902, 1996.
- 573 Zabel, F., Mauser, W., Marke, T., Pfeiffer, A., Zängl, G. and Wastl, C.: Inter-comparison of two land-surface models applied  
574 at different scales and their feedbacks while coupled with a regional climate model, *Hydrology and Earth System  
575 Sciences.*, 16(3), 1017-1031, 2012.
- 576 Zhang, Y., Suzuki, K., Kadota, T. and Ohata, T.: Sublimation from snow surface in southern mountain taiga of eastern  
577 Siberia, *Journal of Geophysical Research: Atmospheres.*, 109(D21), 2004.
- 578 Zhou, J., Pomeroy, J. W., Zhang, W., Cheng, G., Wang, G., and Chen, C.: Simulating cold regions hydrological processes  
579 using a modular model in the west of China, *Journal of Hydrology.*, 509, 13-24, 2014.
- 580